On Nonlinear Model Predictive Control for Energy-Efficient Torque-Vectoring

Alberto Parra, Davide Tavernini, Patrick Gruber, Aldo Sorniotti, *Member, IEEE*, Asier Zubizarreta, and Joshué Pérez, *Member, IEEE*

***Abstract*—A recently growing literature discusses the topics of direct yaw moment control based on model predictive control (MPC), and energy-efficient torque-vectoring (TV) for electric vehicles with multiple powertrains. To reduce energy consumption, the available TV studies focus on the control allocation layer, which calculates the individual wheel torque levels to generate the total reference longitudinal force and direct yaw moment, specified by higher level algorithms to provide the desired longitudinal and lateral vehicle dynamics. In fact, with a system of redundant actuators, the vehicle-level objectives can be achieved by distributing the individual control actions to minimize an optimality criterion, e.g., based on the reduction of different power loss contributions. However, preliminary simulation and experimental studies – not using MPC – show that further important energy savings are possible through the appropriate design of the reference yaw rate. This paper presents a nonlinear model predictive control (NMPC) implementation for energy-efficient TV, which is based on the concurrent optimization of the reference yaw rate and wheel torque allocation. The NMPC cost function weights are varied through a fuzzy logic algorithm to adaptively prioritize vehicle dynamics or energy efficiency, depending on the driving conditions. The results show that the adaptive NMPC configuration allows stable cornering performance with lower energy consumption than a benchmarking fuzzy logic TV controller using an energy-efficient control allocation layer.**

***Index Terms*—Torque-vectoring, nonlinear model predictive control, powertrain power loss, tire slip power loss, reference yaw rate, control allocation, weight adaptation.**

I. Introduction

ELECTRIC vehicles (EVs) are the subject of intensive research as they are considered a key solution to reduce air pollution caused by road traffic. However, the limited driving range has been so far one of the main technical constraints to the widespread adoption of EVs. The issue is being addressed through the enhancement of battery technologies [1], as well as the introduction of superfast charging stations on the road network [2], [3]. In parallel, the efforts to increase driving range are supported by the improvement of the energy efficiency of electric powertrain components, and new vehicle controllers, such as predictive energy management and optimal speed profiling [4].

EVs with multiple powertrains allow torque-vectoring (TV), i.e., individual wheel torque control to produce different longitudinal tire forces on each EV side and, in turn, to generate a so-called direct yaw moment. A wide literature shows the vehicle dynamics benefits of TV in terms of handling and cornering stability, see [5]–[15]. The variety of proposed TV algorithms includes feedforward and proportional integral derivative (PID) controllers [12], H_∞ controllers [15], sliding mode controllers [16], [17], linear quadratic controllers [18], and intelligent controllers [19]. Owing to the increasing computational capabilities of recent embedded platforms, model predictive control (MPC) has become a viable solution for TV [20]–[22], even if many of the available MPC TV implementations still use rather simplified linearized or nonlinear prediction models.

TV can also improve energy efficiency. In fact, the wheel torque distribution has an effect on the electric powertrain power losses, including inverter, electric machine and mechanical transmission (if present) power losses, as well as on the longitudinal and lateral tire slip power losses, i.e., the power losses associated with the longitudinal and lateral slip of the tires [23]–[25]. Most of the available studies on energy-efficient TV focus on multi-layer control structures [26]–[29], in which: a) a top layer generates the total reference longitudinal force and direct yaw moment to achieve a target yaw rate, independently from any energy-efficiency consideration; and b) a bottom layer, or control allocation layer, calculates the individual wheel torque demands to meet the requests from the top layer, e.g., see [30]–[36]. Given the redundancy of the electric powertrains, the individual wheel torque distribution in b) can optimize a secondary optimality criterion, for instance, related to energy consumption. Some of the control allocation implementations use MPC [28], [29].

Although the previous hierarchical arrangements are easy to implement because of their modularity, they do not benefit from the energy consumption effect of the top level controller. This is

Manuscript received January 21, 2020; revised June 10, 2020 and July 28, 2020; accepted August 21, 2020. Date of publication September 4, 2020; date of current version February 12, 2021. This work was supported in part by the Horizon 2020 Programme of the European Commission under Grant Agreements 769944 (STEVE project) and 824311 (ACHILES project). The review of this article was coordinated by Dr. Dongpu Cao. *(Corresponding author: Aldo Sorniotti.)*

Alberto Parra is with Tecnalia Research and Innovation, Basque Research and Technology Alliance, 20009 Donostia-San Sebastián, Spain, with the University of Surrey, Guildford GU2 7XH, U.K., and also with the University of the Basque Country, 48013 Bilbao, Spain (e-mail: alberto.parra@tecnalia.com).

Davide Tavernini, Patrick Gruber, and Aldo Sorniotti are with the University of Surrey, Guildford GU2 7XH, U.K. (e-mail: d.tavernini@surrey.ac.uk; p.gruber@surrey.ac.uk; a.sorniotti@surrey.ac.uk).

Asier Zubizarreta is with the University of the Basque Country, 48013 Bilbao, Spain (e-mail: asier.zubizarreta@ehu.eus).

Joshué Pérez is with Tecnalia Research and Innovation, Basque Research and Technology Alliance, 20009 Donostia-San Sebastián, Spain (e-mail: joshue.perez@tecnalia.com).

Digital Object Identifier 10.1109/TVT.2020.3022022

a major limitation, as recent experimental and simulation-based research work, see [23], [24] and [37], shows that, during cornering, the level of vehicle understeer (typically decided by the top layer of the TV control structure) can have an equivalent impact on the energy consumption as the control allocation algorithm. The preliminary studies on this topic: i) discuss the potential of enhancing energy efficiency by modifying the cornering response through appropriate direct yaw moment characteristics (energy-efficient direct yaw moment control); ii) evaluate the impact of these techniques on powertrain and tire slip power losses; and iii) obtain suboptimal rule-based or open-loop algorithms. However, they do not propose systematic solutions based on nonlinear optimal control. For example, Kobayashi *et al.* [24] demonstrate that the minimization of the tire slip power losses occurs if the tire slip velocity vectors are the same at the four vehicle corners. De Filippis *et al.* [38] obtain an analytical expression of the energy-efficient direct yaw moment in terms of powertrain power losses, implying the activation of an increasing number of powertrains with increasing torque demand. In case of redundant optimal solutions from the viewpoint of powertrain power losses, rules are set to select the best option in terms of tire slip power losses. A quasi-static vehicle modeling approach is used in [39] to derive rules for the calculation of a feedforward energy-efficient direct yaw moment as a function of torque demand, with a feedback contribution intervening only in safety-critical conditions.

Although the previous studies show the energy saving potential of shaping the reference cornering response, to be practically useful, the implementation of this approach should: i) simultaneously account for the power losses associated with the powertrains and tire slip; ii) be based on feedback control structures, e.g., capable of compensating unexpected EV behavior caused by the variation of system parameters or transients, rather than using simplified feedforward or rule-based algorithms; iii) integrate the reference direct yaw moment generation and control allocation functions, to prevent conflicts between different control layers involved in the power loss management; and iv) provide significant operational flexibility depending on the actual driving situation, i.e., prioritize energy efficiency during normal driving, and vehicle safety and stability in extreme maneuvers. In conclusion, to the best of the authors' knowledge, there is lack of TV control implementations systematically using the reference cornering response as a control variable to reduce energy consumption.

This study covers the identified gap, with the following novel contributions:

- An implicit nonlinear model predictive control (NMPC) implementation, integrating the direct yaw moment calculation layer with the control allocation layer, and including consideration of the yaw rate tracking performance, energy-efficient cornering response, and sideslip and actuation constraints.
- The systematic adoption of an energy-efficient reference yaw rate, i.e., the yaw rate to be tracked by the NMPC in normal driving conditions provides an energy-efficient cornering response, while a fuzzy-logic based adaptation mechanism mediates between the requirements of vehicle stability and energy efficiency.
- An analysis of the relative significance of energy-efficient understeer characteristics and control allocation, as well as the benefit of considering the power loss aspects within feedback controllers, rather than through feedforward algorithms.

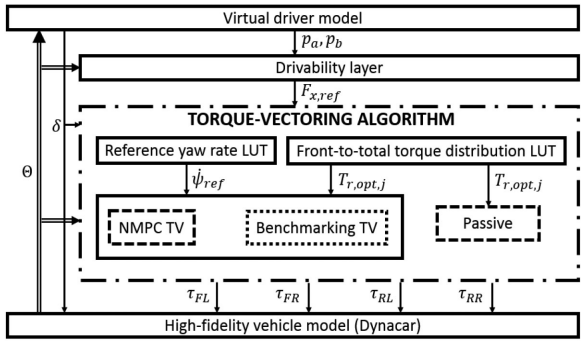

Fig. 1. Schematic of the implemented simulation framework.

The manuscript is organized into six sections. Section II presents the simulation framework for the control system evaluation. Section III describes the off-line generation process of the reference yaw rate characteristics and rear-to-total torque distribution. Section IV covers the integrated and adaptive NMPC formulation for energy-efficient TV. Section V discusses the results, and compares the proposed approach with a benchmarking TV controller from the literature. Finally, Section VI summarizes the main conclusions.

II. Simulation Framework and High-Fidelity Simulation Model

A. Simulation framework

The simulation framework, shown in Fig. 1, consists of:

- The virtual driver model, which tracks the reference speed and path.
- The drivability layer, which converts the driver inputs on the accelerator and brake pedals, p_a and p_b, into the total longitudinal force demand for the electric powertrains, $F_{x,ref}$ (the actuation of the friction brakes is beyond the scope of this study).
- The TV layer, which generates the individual powertrain torque values, τ_{ij}, where the subscript $i = F, R$ indicates the front or rear axles, and the subscript $j = L, R$ indicates the left or right sides. The main contribution of this work is the NMPC TV approach (see Section IV) of this layer, which: i) uses the energy-efficient reference yaw rate and (when appropriate) rear-to-total torque distribution, $T_{r,ref,j}$, which will be defined in Section III; ii) considers the different relevant power loss contributions from the powertrains and tires; and iii) includes a fuzzy logic algorithm for prioritizing its objectives depending on the driving conditions. As alternatives to the NMPC TV approach, the TV layer also includes: a) a 'Passive'

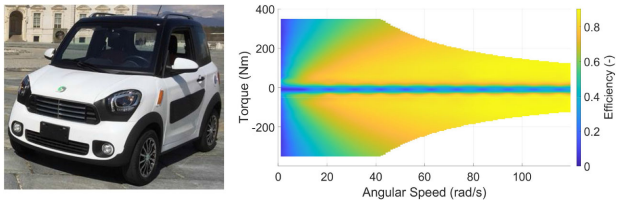

Fig. 2. Case study vehicle (left) and the experimentally measured efficiency map of the installed powertrains (right).

TABLE I
MAIN VEHICLES PARAMETERS

Symbol	Description and unit	Value
m	Vehicle mass (kg)	649
R	Tire radius (m)	0.2625
h	Center of gravity (CoG) height (m)	0.4
d	Track width	1.33
l_F	Distance from front axle to CoG (m)	0.99
l_R	Distance from rear axle to CoG (m)	0.825
l	Wheelbase (m)	1.815
I_x	Roll mass moment of inertia (kg m^2)	200
I_y	Pitch mass moment of inertia (kg m^2)	300
I_z	Yaw mass moment of inertia (kg m^2)	400

implementation, which implies zero direct yaw moment, i.e., the reference longitudinal force is evenly distributed among the two EV sides; and b) a benchmarking TV controller (see Section V.B), based on fuzzy logic.

- The high-fidelity vehicle dynamics simulation model (see Section II.B), receiving the steering input from the driver and wheel torque demands from the TV layer, and generating the set of vehicle variables, Θ, for the operation of the TV system and virtual driver.

B. High-Fidelity Vehicle Model and Case Study EV

The adopted high-fidelity vehicle dynamics simulation tool is Dynacar, developed by Tecnalia, and experimentally validated on multiple vehicles, see [40]–[42]. The model includes the degrees of freedom of the sprung and unsprung masses, and considers suspension kinematics. The multibody approach is based on [43], using one coordinate for each degree of freedom through macro-joints, which leads to high computational efficiency. The tire forces are modeled with the Pacejka magic formula, version 2006 [44].

The case study vehicle is the four-wheel-drive variant of a lightweight EV being developed within the European Horizon 2020 STEVE project. Fig. 2 shows the reference EV, together with the measured in-wheel direct drive powertrain efficiency map (the same at each corner), provided by the manufacturer, Elaphe Propulsion Technologies Ltd [45]. Relevant EV parameters are reported in Table I, and Fig. 3 defines the sign conventions of the main variables.

III. ENERGY-EFFICIENT REFERENCE YAW RATE AND REAR-TO-TOTAL TORQUE DISTRIBUTION

In accordance with Fig. 1, the definition of the energy-efficient reference rear-to-total wheel torque distribution and yaw rate characteristics is the first step in the control design process.

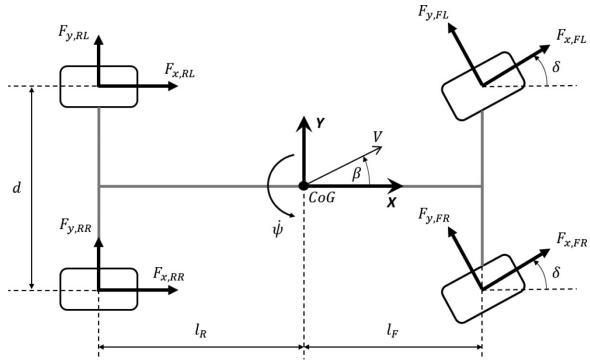

Fig. 3. Top view of the vehicle with indication of the sign conventions for the main variables.

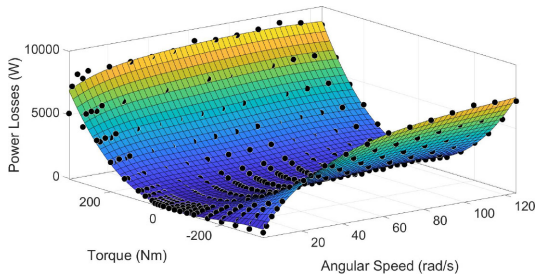

Fig. 4. Experimental power loss characteristic of the case study individual in-wheel powertrain as a function of torque and speed (the dots indicate the measurement points), and its approximation adopted within the NMPC formulation.

A. Power Loss Contributions

In this study, the relevant sources of power loss are the powertrains, because of their efficiency characteristics, and the tires, because of their longitudinal and lateral slips. The aerodynamic drag is also a source of power loss, but is not affected by the proposed NMPC TV, as the case study EV does not feature any system that controls this variable. Likewise, the rolling resistance of the tires is a source of power loss that cannot be influenced by the TV control action, as it mainly depends on the tire properties and inflation pressure [44]. Based on this, (1) defines the total power loss contribution, $P_{Loss,tot}$, that is reduced by the proposed NMPC TV:

$$P_{Loss,tot} = P_{Loss,PWT} + P_{Loss,Tire,Long} + P_{Loss,Tire,Lat} \tag{1}$$

where $P_{Loss,PWT}$ is the total powertrain power loss, and $P_{Loss,Tire,Long}$ and $P_{Loss,Tire,Lat}$ are the total longitudinal and lateral slip power losses of the tires. For energy-efficient reference yaw rate design and control assessment, the calculation of the power loss contributions is carried out by the Dynacar model.

The individual in-wheel powertrain power losses, $P_{Loss,PWT,ij}$ (see Fig. 4) are determined from the powertrain efficiency map, $\eta_{ij}(\tau_{ji}, \omega_{ij})$, reported in Fig. 2:

$$P_{Loss,PWT,ij} = \left\{ \begin{array}{l} \tau_{ij}\omega_{ij}\left[\frac{1}{\eta_{ij}(\tau_{ij},\omega_{ij})} - 1\right], \ \tau_{ij} > 0 \\ \tau_{ij}\omega_{ij}\left[\eta_{ij}\left(\tau_{ij},\omega_{ij}\right) - 1\right], \ \tau_{ij} < 0 \\ P_{Loss,PWT,res,ij}\left(\omega_{ij}\right), \ \tau_{ij} = 0 \end{array} \right\} \tag{2}$$

where τ_{ij} is the torque demand of the ij machine; ω_{ij} is the angular speed of the ij wheel; and $P_{Loss,PWT,res,ij}$ is the power loss of the ij powertrain when this is switched off, caused by the cogging loss and mechanical loss contributions. Hence, at the vehicle level, the total powertrain power loss, $P_{Loss,PWT}$, is given by:

$$P_{Loss,PWT} = \sum_{\substack{i=F,R \\ j=R,L}} P_{Loss,PWT,ij} \tag{3}$$

The total longitudinal tire slip power losses, $P_{Loss,Tire,Long}$, are given by:

$$P_{Loss,Tire,Long} = \sum_{\substack{i=F,R \\ j=R,L}} F_{x,ij} V_{slip,x,ij} \tag{4}$$

where $F_{x,ij}$ is the longitudinal tire force at the ij corner; and $V_{slip,x,ij}$ is the longitudinal slip speed of the respective tire:

$$V_{slip,x,ij} = \omega_{ij} R - V_{x,ij} \tag{5}$$

R is the tire rolling radius, and $V_{x,ij}$ is the longitudinal component of the linear wheel speed in the tire reference system.

The total lateral tire slip power losses are given by:

$$P_{Loss,Tire,Lat} = \sum_{\substack{i=F,R \\ j=R,L}} F_{y,ij} V_{slip,y,ij} \tag{6}$$

where $F_{y,ij}$ is the lateral tire force at the ij corner; and $V_{slip,y,ij}$ is the lateral slip speed of the respective tire:

$$V_{slip,y,ij} = -V_{x,ij} \tan \alpha_{ij} \tag{7}$$

B. Energy-Efficient Rear-to-Total Wheel Torque Distribution

Within each EV side, the rear-to-total wheel torque distribution ratio, $T_{r,j}$, is defined as:

$$T_{r,j} = \frac{\tau_{Rj}}{\tau_{Fj} + \tau_{Rj}} \tag{8}$$

An off-line brute force algorithm calculates the value of $T_{r,j}$ that maximizes the total powertrain efficiency, $\eta_{tot,j}$, on the j vehicle side:

$$T_{r,opt,j} = \arg_{T_{r,j}} \max \eta_{tot,j} \tag{9}$$

$\eta_{tot,j}$ is the ratio of the total powertrain output power, $P_{out,j}$, to the total powertrain input power, $P_{in,j}$, on the considered vehicle side; in particular, in traction conditions, the mathematical definition of $\eta_{tot,j}$, based on the efficiency of the two powertrains on the j side, is:

$$\begin{aligned} \eta_{tot,j} &= \eta_{tot,j}\left(T_{r,j}, \tau_{req,j}, \omega_{Fj}, \omega_{Rj}\right) \\ &= \frac{P_{out,j}\left(T_{r,j}, \tau_{req,j}, \omega_{Fj}, \omega_{Rj}\right)}{P_{in,j}\left(T_{r,j}, \tau_{req,j}, \omega_{Fj}, \omega_{Rj}\right)} \\ &= \frac{\left[1 - T_{r,j}\right] \tau_{req,j} \omega_{Fj} + T_{r,j} \tau_{req,j} \omega_{Rj}}{\frac{[1-T_{r,j}]\tau_{req,j}}{\eta_{Fj}([1-T_{r,j}]\tau_{req,j}, \omega_{Fj})} \omega_{Fj} + \frac{T_{r,j}\tau_{req,j}}{\eta_{Rj}(T_{r,j}\tau_{req,j}, \omega_{Rj})} \omega_{Rj}} \end{aligned} \tag{10}$$

where $\tau_{req,j} = \tau_{Fj} + \tau_{Rj}$.

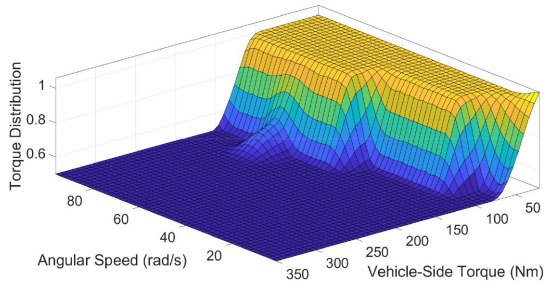

Fig. 5. Energy-efficient rear-to-total wheel torque distribution ratio as a function of vehicle side torque and speed.

The brute force algorithm works under a zero tire slip ratio assumption, i.e., $\omega_{F,j} = \omega_{Rj} \approx V/R$, where V is vehicle speed. The output is a look-up table of $T_{r,opt,j} = T_{r,opt,j}(\tau_j, V/R)$, used for the design of the vehicle controllers. Fig. 5 shows the optimization result, which is consistent with the one in [31]. For a given speed, low torque demand values ($< 100 \sim 150$ Nm) on the EV side imply that only one powertrain is active, while at medium-to-high side torque demands $T_{r,opt,j}$ is 0.5, indicating an even torque distribution among the powertrains within the same EV side. The transition between the two conditions occurs progressively, at a torque level varying with speed.

In the NMPC TV implementations of this study, the reference rear-to-total distribution ratios, $T_{r,ref,j}$, are defined according to the approach in [31]:

$$T_{r,ref,j} = \xi_1 \ + 0.5 \ (\xi_2 - \xi_3) \left\{1 + \tanh\left(\xi_4 \left[\tau_{req,j} - \xi_5\right]\right)\right\} \tag{11}$$

where (11) is set to follow the profile defined by the map in Fig. 5, through appropriate parametrization of the coefficients $\xi_1, \ldots, \xi_5$, as a function of the current vehicle speed.

C. Reference Understeer Characteristics

This subsection: i) discusses the effect of the vehicle understeer characteristic on energy consumption; and ii) derives the set of energy-efficient understeer characteristics used for the generation of the reference yaw rate of the TV controller.

To obtain the optimal understeer characteristics, ramp steer maneuvers with slow steering input ramps at constant EV speed were simulated with the Dynacar model. The maneuvers were repeated with different constant direct yaw moment values, ranging from -900 Nm to +900 Nm in steps of 100 Nm, using the rear-to-total torque distribution map in Fig. 5 within each EV side. Also, to emulate the cornering response with non-zero longitudinal acceleration, a_x, at a given speed, ramp steer tests were performed with a constant longitudinal force applied to the EV's center of gravity.

Figs. 6 and 7 are examples of results at $V = 60$ km/h and a tire-road friction coefficient $\mu = 0.9$. For each lateral acceleration a_y, Fig. 6 reports the understeer characteristics (in terms of dynamic steering angle, δ_{dyn}, see [46], [47] for the theory) of the case study EV with: a) even torque distribution among all wheels. This characteristic is indicated as "Passive" in the plot; and b) the energy-efficient rear-to-total torque distribution

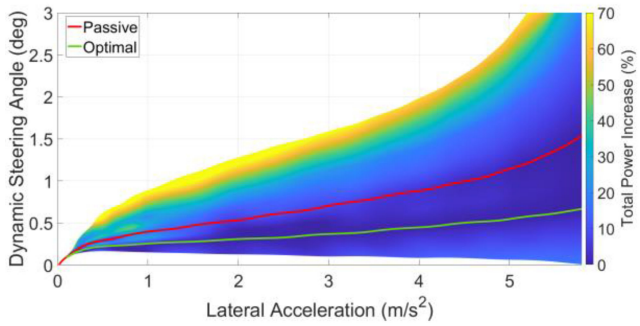

Fig. 6. Example of % variation of the powertrain power input with the understeer characteristic ($V = 60$ km/h, $\mu = 0.9$).

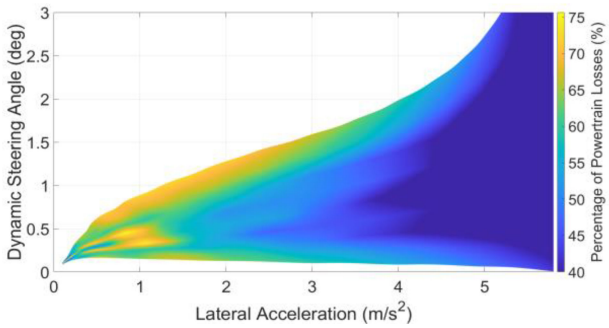

Fig. 7. Example of % significance of the powertrain power loss with respect to the total TV-affected power loss ($V = 60$ km/h, $\mu = 0.9$).

ratio within each side, and the optimal direct yaw moment within the considered range, i.e., the one minimizing the power consumption for a given a_y, based on the simulations. The resulting understeer characteristic is indicated as "Optimal" in the plot.

The color scale in Fig. 6, obtained by interpolating the ramp steer results, shows the percentage increment of the powertrain power input, $P_{in,incr,\%}$, for a generic point (δ_{dyn}, a_y), with respect to the optimal condition at the same a_y:

$$P_{in,incr,\%}\left(\delta_{dyn}, a_y\right) = 100\frac{P_{in}\left(\delta_{dyn}, a_y\right) - P_{in,opt}\left(a_y\right)}{P_{in,opt}\left(a_y\right)} \tag{12}$$

where $P_{in}(\delta_{dyn}, a_y)$ is the total input power at the dynamic steering angle δ_{dyn} and lateral acceleration a_y, while $P_{in,opt}$ is the minimum input power at the specific a_y.

The influence of the understeer characteristic on the EV energy consumption is major, with peak values of $P_{in,incr,\%}$ in excess of 50%. In particular, the average difference between the Passive and Optimal configurations amounts to 6.62% for the considered a_y range.

The important conclusion is that an energy-efficient TV controller must include appropriate design of the reference understeer characteristic, and hence the reference yaw rate. Moreover, an energy-efficient TV controller should also be able to determine the most appropriate reference yaw rate in transient conditions, thus going beyond the results in Fig. 6, based on quasi-steady-state cornering conditions.

Fig. 7 shows the significance of the powertrain power loss over the total power loss that can be affected by TV, through the $P_{Loss,\%}$ parameter, indicated by the color scale of the graph:

$$P_{Loss,\%}\left(\delta_{dyn}, a_y\right) = 100\frac{P_{Loss,PWT}}{P_{Loss,tot}}$$
$$= 100\frac{P_{Loss,PWT}}{P_{Loss,PWT} + P_{Loss,Tire,Long} + P_{Loss,Tire,Lat}} \tag{13}$$

At low a_y, the contribution of the electric powertrains is the most important one, and it accounts for up to 75% of the total relevant power loss. With increasing a_y, the relative powertrain power loss contribution progressively reduces, and, above 5 m/s^2, becomes less than 50% of the total TV-affected power loss. This observation implies that an energy-efficient TV controller should consider all indicated sources of power loss, as each of them could become predominant depending on the operating condition.

The analysis of Figs. 6 and 7 was repeated for different vehicle speeds, emulated longitudinal accelerations, and tire-road friction coefficients, which resulted in a set of energy-efficient reference understeer characteristics, expressed as a four-dimensional map, $\delta_{dyn,ref}(a_y, a_x,\ V,\ \mu)$.

D. Energy-Efficient Reference Yaw Rate

The energy-efficient understeer characteristics, $\delta_{dyn,ref}(a_y, a_x,\ V,\ \mu)$, can be expressed in terms of actual steering angle, $\delta_{ref}(a_y, a_x,\ V,\ \mu)$, as:

$$\delta_{ref}\left(a_y, a_x,\ V,\ \mu\right) = \delta_{dyn,ref}\left(a_y, a_x,\ V,\ \mu\right) + \frac{l a_y}{V^2} \tag{14}$$

Through manipulation of $\delta_{ref}(a_y, a_x,\ V,\ \mu)$, and considering the relationship between a_y and $\dot{\psi}$, the nominal energy-efficient reference yaw rate maps are obtained, in terms of $\dot{\psi}_{ref,nom}(\delta, a_x,\ V,\ \mu)$. Fig. 8 reports examples of energy-efficient reference yaw rate profiles as functions of steering wheel angle, for different values of vehicle speed, longitudinal acceleration, and tire-road friction coefficient. While the dependency on V and μ is evident, the effect of a_x is rather limited for the studied longitudinal acceleration values, corresponding to normal driving conditions.

With appropriate first-order filtering to achieve the desired reference dynamics, the nominal reference yaw rate characteristics are used to calculate the reference yaw rate, $\dot{\psi}_{ref}$, given as input to the TV controller described in Section IV. However, the NMPC will be designed to allow deviations from $\dot{\psi}_{ref}$, as during transients or EV operation with non-nominal parameters, the reference yaw rate calculated off-line can be different from the most energy-efficient yaw rate.

IV. Nonlinear Model Predictive Controller for Energy-Efficient Torque-Vectoring

A. Control Structure

The overall NMPC TV structure is shown in Fig. 9. The inputs are: i) the total force demand, $F_{x,ref}$; ii) the steering angle, δ; iii) the energy-efficient reference yaw rate, $\dot{\psi}_{ref}$, discussed in

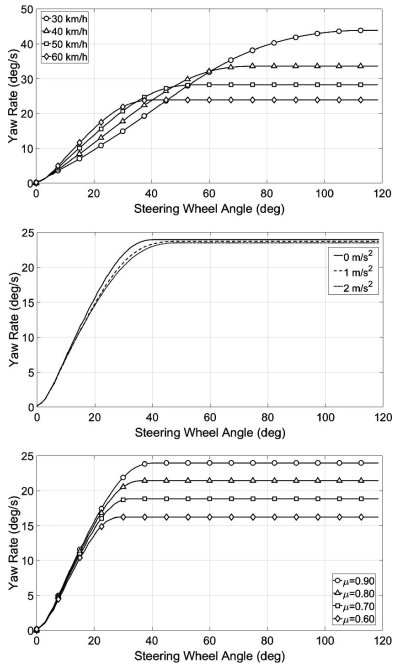

Fig. 8. Examples of nominal energy-efficient reference yaw rate profiles as functions of steering wheel angle, for different values of vehicle speed, longitudinal acceleration, and tire-road friction coefficient.

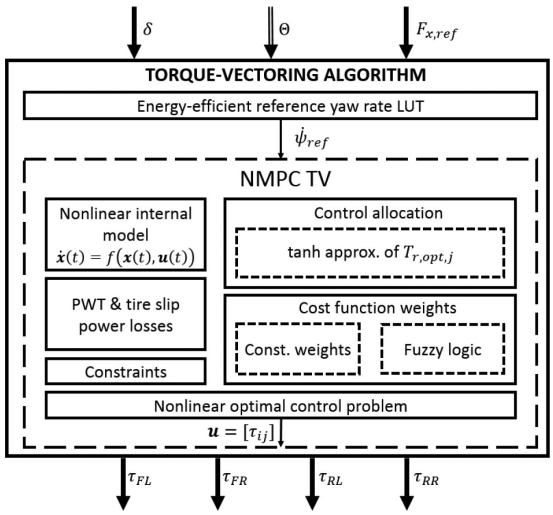

Fig. 9. Simplified block diagram of the NMPC TV system.

Section III; and iv) the estimated variables and vehicle parameters, organized in the vector Θ. The outputs are the individual torque demands, τ_{ij}.

B. Internal Model Formulation

The internal NMPC model is expressed through the following continuous time formulation [48]:

$$\dot{\boldsymbol{x}}\ (t) = f\left(\boldsymbol{x}\left(t\right), \boldsymbol{u}\left(t\right)\right) \tag{15}$$

where the state vector $\boldsymbol{x}$ is:

$$\boldsymbol{x} = \left[V\ \beta\ \dot{\psi}\ \omega_{FL}\ \omega_{FR}\ \omega_{RL}\ \omega_{RR}\right]^T \tag{16}$$

$\boldsymbol{x}$ is also part of Θ (see Fig. 1), and its current value, $\boldsymbol{x_{in}}$, result of the on-board measurements and state estimation, is provided to the controller at each time step, as initial condition for the prediction based on the internal model. The control action is defined as:

$$\boldsymbol{u} = \left[\tau_{FL}\ \tau_{FR}\ \tau_{RL}\ \tau_{RR}\right]^T \tag{17}$$

Similarly to some of the recent NMPC implementations for TV [20], the prediction model formulation (15) includes 7 degrees of freedom, described by the following force and moment balance equations.

- Longitudinal force balance:

$$\begin{aligned}\dot{V} = \frac{1}{m}\ \{&[F_{x,FL} + F_{x,FR}]\cos\left(\delta - \beta\right) \\ &- [F_{y,FL} + F_{y,FR}]\sin\left(\delta - \beta\right) + \ [F_{x,RL} + F_{x,RR}] \\ &\times \cos\beta + \ [F_{y,RL} + F_{y,RR}]\sin\beta\}\end{aligned} \tag{18}$$

- Lateral force balance:

$$\begin{aligned}\dot{\beta} = \frac{1}{mV}\ \{&[F_{x,FL} + F_{x,FR}]\sin\left(\delta - \beta\right) \\ &+ [F_{y,FL} + F_{y,FR}]\cos\left(\delta - \beta\right) - [F_{x,RL} + F_{x,RR}] \\ &\times \sin\beta + [F_{y,RL} + F_{y,RR}]\cos\beta\} - \dot{\psi}\end{aligned} \tag{19}$$

- Yaw moment balance:

$$\begin{aligned}\ddot{\psi} = \\ \frac{1}{I_z}\Big\{&[F_{x,FL}+F_{x,FR}]\,l_F\sin\delta+[F_{y,FL}+F_{y,FR}]\,l_F\cos\delta \\ &- [F_{y,RL} + F_{y,RR}]\,l_R + \left[F_{x,FR}\cos\delta\right. \\ &\left. - F_{y,FR}\sin\delta + F_{x,RR}\right]\frac{d}{2} \\ &- \left[F_{x,FL}\cos\delta - F_{y,FL}\sin\delta + F_{x,RL}\right]\frac{d}{2}\Big\}\end{aligned} \tag{20}$$

- ij wheel moment balance:

$$I_\omega\dot{\omega}_{ij} = \tau_{ij} - F_{x,ij}R \tag{21}$$

where β is the sideslip angle and I_ω is the mass moment of inertia of the wheel. Aerodynamic drag and tire rolling resistance are neglected, as they are not affected at the overall EV level by the wheel torque distribution.

The longitudinal and lateral tire forces, $F_{x,ij}$ and $F_{y,ij}$, are given by the product of the respective tire force coefficient, $\mu_{x,ij}$ and $\mu_{y,ij}$, by the vertical tire load, $F_{z,ij}$:

$$F_{x,ij} = \mu_{x,ij}F_{z,ij} \tag{22}$$

$$F_{y,ij} = \mu_{y,ij}F_{z,ij} \tag{23}$$

A simplified version of the Pacejka magic formula has been used, which determines the resultant total tire force coefficient, μ_{ij}:

$$\mu_{ij}\left(s_{ij}\right) = \mathrm{MF}\left(s_{ij}\right) = D\sin\left(C\mathrm{atan}\left(Bs_{ij}\right)\right) \tag{24}$$

where MF indicates the magic formula; B, C and D are constant magic formula coefficients, calculated to match the actual tire characteristics; and the total slip, s_{ij}, results from the composition of the longitudinal and lateral slip components, $s_{x,ij}$ and

$s_{y,ij}$:

$$s_{ij} = \sqrt{s_{x,ij}^2 + s_{y,ij}^2} \tag{25}$$

$s_{x,ij}$ is defined as:

$$s_{x,ij} = \frac{V_{slip,x,ij}}{\omega_{ij} R} \tag{26}$$

and $s_{y,ij}$ is given by:

$$s_{y,ij} = \frac{V_{slip,y,ij}}{\omega_{ij} R} \tag{27}$$

where the linear longitudinal and lateral slip speeds, $V_{slip,x,ij}$ and $V_{slip,y,ij}$, are defined in (5) and (7). In the calculation of $V_{slip,y,ij}$, simplified linearized expressions are adopted for the tire slip angles α_{ij}:

$$\begin{cases} \alpha_{FL} \approx \alpha_{FR} \approx -\delta + \beta + \frac{\dot{\psi} l_F}{V} \\ \alpha_{RL} \approx \alpha_{RR} \approx \beta - \frac{\dot{\psi} l_R}{V} \end{cases} \tag{28}$$

The longitudinal and lateral tire load coefficients, $\mu_{x,ij}$ and $\mu_{y,ij}$, are obtained by decomposing the tire load coefficient from (24) according to the slip components.

$$\mu_{x,ij} = \frac{s_{x,ij}}{s_{ij}} \ \mu_{ij} \tag{29}$$

$$\mu_{y,ij} = \frac{s_{y,ij}}{s_{ij}} \ \mu_{ij} \tag{30}$$

The adopted tire model is a simple yet realistic formulation, easy to tune and independent from the specific complete set of Pacejka magic formula coefficients of the high-fidelity plant model in Section II.B. The NMPC feedback set-up based on the receding horizon approach tends to compensate for the inevitable tire model mismatches, which – in any case – would characterize the implementation on a real vehicle.

$F_{z,ij}$ is calculated as the sum of the static load, $F_{z,ij}^0$, longitudinal load transfer, ΔF_z^x, and lateral load transfer, $\Delta F_{z,i}^y$:

$$\begin{cases} F_{z,FL} = F_{z,FL}^0 - \Delta F_z^x - \Delta F_{z,F}^y \\ F_{z,FR} = F_{z,FR}^0 - \Delta F_z^x + \Delta F_{z,F}^y \\ F_{z,RL} = F_{z,RL}^0 + \Delta F_z^x - \Delta F_{z,R}^y \\ F_{z,RR} = F_{z,RR}^0 + \Delta F_z^x + \Delta F_{z,R}^y \end{cases} \tag{31}$$

where the static loads are:

$$\begin{cases} F_{z,FL}^0 = F_{z,FR}^0 = \frac{1}{2} \ mg \frac{l_R}{l_F + l_R} \\ F_{z,RL}^0 = F_{z,RR}^0 = \frac{1}{2} \ mg \frac{l_F}{l_F + l_R} \end{cases} \tag{32}$$

The longitudinal load transfer is given by:

$$\Delta F_z^x = \frac{1}{2} \ \frac{m \, h \, a_x}{l_F + l_R} \tag{33}$$

while the front and rear lateral load transfers are given by:

$$\begin{cases} \Delta F_{z,F}^y = \frac{m \, a_y}{d} \left[\frac{h_{RC} \, l_R}{l_F + l_R} + \gamma h_{Roll} \right] \\ \Delta F_{z,R}^y = \frac{m \, a_y}{d} \left\{ \frac{h_{RC} \, l_F}{l_F + l_R} + [1 - \gamma] \, h_{Roll} \right\} \end{cases} \tag{34}$$

where h_{RC} is the roll center height, h_{Roll} is the distance between the center of gravity and the roll axis, and γ is the front-to-total suspension roll stiffness distribution.

Within the NMPC prediction model, the tire slip power losses are obtained through (4) and (6), while a polynomial formulation is used for the electric powertrain power losses:

$$P_{loss,PWT} = \sum_{\substack{i=F,R \\ j=R,L}} \begin{bmatrix} p_{00} + p_{10}\tau_{ij} + p_{01}\omega_{ij} + p_{20}\tau_{ij}^2 + p_{11}\tau_{ij}\omega_{ij} \\ + p_{02}\omega_{ij}^2 + p_{30}\tau_{ij}^3 + p_{21}\tau_{ij}^2\omega_{ij} + p_{12}\tau_{ij}\omega_{ij}^2 \\ + p_{03}\omega_{ij}^3 + p_{40}\tau_{ij}^4 + p_{31}\tau_{ij}^3\omega_{ij} \\ + p_{22}\tau_{ij}^2\omega_{ij}^2 + p_{13}\tau_{ij}\omega_{ij}^3 + p_{04}\omega_{ij}^4 + p_{50}\tau_{ij}^5 \\ + p_{41}\tau_{ij}^4\omega_{ij} + p_{32}\tau_{ij}^3\omega_{ij}^2 + p_{23}\tau_{ij}^2\omega_{ij}^3 \\ + p_{14}\tau_{ij}\omega_{ij}^4 + p_{05}\omega_{ij}^5 \end{bmatrix} \tag{35}$$

(35) provides a good approximation of the experimental power loss characteristic, defined in (2), see Fig. 4; in fact, with the adopted parametrization, the root mean square (RMS) of the power loss error across the operating range of the motor is 75 W.

C. Optimal Control Problem Formulation

The idea of nonlinear model predictive control is to use a model of the plant to predict and optimize the future system behavior. This optimization is achieved by applying a control action, which is obtained by solving, at each sampling instant, a finite horizon optimal control problem, using the current state of the plant. The optimization yields an optimal control sequence, and the first control in this sequence is applied to the plant.

The proposed NMPC control law minimizes the cost function J, subject to appropriate equality and inequality constraints. The optimal control problem is defined in discrete time as:

$$\begin{aligned} &\min_{\boldsymbol{u}} \ J\left(\boldsymbol{x}\left(0\right), \boldsymbol{u}\left(\cdot\right)\right) := \ell_N\left(\boldsymbol{x}\left(N\right)\right) + \sum_{k \, = \, 0}^{N-1} \ell\left(\boldsymbol{x}\left(k\right), \boldsymbol{u}\left(k\right)\right) \\ &\text{s.t. } \boldsymbol{x}\left(0\right) = \boldsymbol{x_{in}} \\ &\quad \boldsymbol{x}\left(k+1\right) = f_d\left(\boldsymbol{x}\left(k\right), \ \boldsymbol{u}\left(k\right)\right) \\ &\quad \underline{\boldsymbol{x}} \leq \boldsymbol{x}\left(k\right) \leq \bar{\boldsymbol{x}} \\ &\quad \underline{\boldsymbol{x}} \leq \boldsymbol{x}\left(N\right) \leq \bar{\boldsymbol{x}} \\ &\quad \underline{\boldsymbol{u}} \leq \boldsymbol{u}\left(k\right) \leq \bar{\boldsymbol{u}} \\ &\quad \boldsymbol{u}\left(\cdot\right) : \ [0, \ N-1] \end{aligned} \tag{36}$$

where $\ell_N(\boldsymbol{x}(N))$ is the terminal cost; N is the number of steps of the prediction horizon H_P, in this implementation equal to the control horizon H_c, i.e., $H_c = H_p \ = \ N \, T_s$, with T_s being the discretization time; k indicates the discretization step; $\underline{\boldsymbol{x}}$ and $\bar{\boldsymbol{x}}$ are the lower and upper limits for $\boldsymbol{x}$; $\underline{\boldsymbol{u}}$ and $\bar{\boldsymbol{u}}$ are the lower and upper limits for $\boldsymbol{u}$; $\boldsymbol{x}(k+1) = \ f_d(\boldsymbol{x}(k), \ \boldsymbol{u}(k))$ is the discretized model defined in (15), detailed in the previous subsection; and $\ell(\boldsymbol{x}(k), \boldsymbol{u}(k))$ is the stage cost function associated to each time step, defined as a least-squares function:

$$\begin{aligned} &\ell\left(\boldsymbol{x}\left(k\right), \boldsymbol{u}\left(k\right)\right) \\ &= W_{u,F_x}\{F_{x,ref} - [F_{x,FL} + F_{x,FR} + F_{x,RL} + F_{x,RR}]\}^2 \\ &\quad + W_{u,\dot{\psi}}\left[\dot{\psi}_{ref} - \dot{\psi}\right]^2 + W_{u,\alpha_R}\alpha_R^2 + W_{u,PWT}{P_{Loss,PWT}}^2 \\ &\quad + W_{u,Tire}[P_{Loss,Tire,Long} + P_{Loss,Tire,Lat}]^2 \end{aligned}$$

$$+ W_{u,LD}\left[\frac{\tau_{RL}}{\tau_{FL}+\tau_{RL}} - T_{r,ref,L}\right]^2$$
$$+ W_{u,LD}\left[\frac{\tau_{RR}}{\tau_{FR}+\tau_{RR}} - T_{r,ref,R}\right]^2 \quad (37)$$

where $F_{x,ref}$ is the total force demand from the drivability controller; α_R is the rear axle slip angle; $P_{Loss,PWT}$ is the total electric powertrain power loss estimated through (35); and $P_{Loss,Tire,Long}$ and $P_{Loss,Tire,Lat}$ are the tire slip power losses calculated through (4), (6), and the simplified version of the magic formula of the internal model.

W_{u,F_x}, $W_{u,\dot{\psi}}$, W_{u,α_R}, $W_{u,PWT}$, $W_{u,Tire}$ and $W_{u,LD}$ are the cost function weights, respectively prioritizing longitudinal force tracking, reference yaw rate tracking, rear axle slip angle reduction, powertrain power loss reduction, tire slip power loss reduction, and rear-to-total torque distribution tracking within each EV side. Given the different range of the variables in (37), each weight is expressed as the ratio of a weighting coefficient (r_{u,F_x}, $r_{u,\dot{\psi}}$, r_{u,α_R}, $r_{u,PWT}$, $r_{u,Tire}$ and $r_{u,LD}$, referring to the different terms of the cost function) to the square of a corresponding scaling factor coefficient (U_{sc,F_x}, $U_{sc,\dot{\psi}}$, U_{sc,α_R}, $U_{sc,PWT}$, $U_{sc,Tire}$ and $U_{sc,LD}$), e.g., $W_{u,F_x} = r_{u,F_x}/U^2_{sc,F_x}$. The scaling factor coefficient represents the maximum expected value of the respective cost function variable, i.e., the squared ratio of the variable factor of each cost function term to the scaling factor coefficient ranges from 0 to 1. This formulation brings equivalent influence of the weighting coefficients, which are thus representative of the level of priority assigned to the cost function terms, and offers ease of controller tunability.

The following state and control action constraints have been implemented in (36) as box constraints (lower and upper limits):

- Yaw rate constraint fixed for the whole prediction horizon, based on the tire-road friction coefficient μ, i.e., $|\dot{\psi}| \leq \mu g/V_{in}$.
- Sideslip angle constraint, i.e., $|\beta| \leq \beta_{max}$, set to 5 deg.
- Individual tire slip ratio constraints, i.e., $|s_{x,ij}| \leq s_{x,max,ij}$, where $s_{x,max,ij}$ is the maximum allowed value of longitudinal slip, set to 0.15 for the simulations of this study.
- Individual wheel torque constraints, i.e., $|\tau_{ij}| \leq \tau_{max,ij}$, where $\tau_{max,ij}$ is the maximum powertrain torque at V_{in}.

D. Controller Implementation and Selection of Prediction Horizon and Time Step

The controller was set up through the ACADO toolkit [49], which can automatically generate code for Gauss-Newton iteration algorithms for fast NMPC with constraints. The selected solver parameters were: multiple shooting discretization method, fourth order Runge Kutta integrator, and qpOASES QP optimization algorithm.

By using the ACADO toolbox, the proposed algorithm has been implemented in real-time on a dSPACE MicroAutoBox II unit, see Fig. 10. A sensitivity analysis was carried out to investigate the effect of the NMPC prediction horizon, H_P, and internal model discretization time, T_S, and identify the best compromise between controller performance and computational effort. H_P ranged from 250 ms to 750 ms, while T_S ranged from 10 ms to 30 ms. The implementation step of the controller, ΔT, i.e., the time step at which the controller updates its outputs, was set to be larger, with appropriate and consistent margin, than the maximum execution time on the available control hardware, and therefore was different for each set of H_P and T_S.

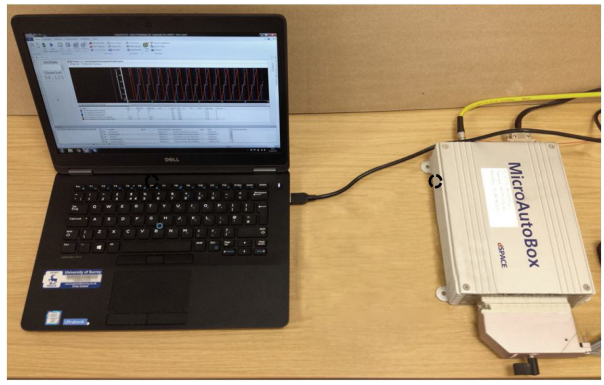

Fig. 10. Implementation set-up for the proposed NMPC TV real-time assessment.

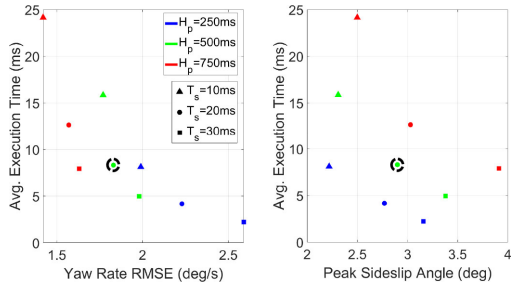

Fig. 11. Effect of H_P and T_S on the average execution time on a dSPACE MicroAutoBox II device: RMS of the yaw rate error, and peak value of sideslip angle, during an obstacle avoidance from an initial speed of 56 km/h.

Fig. 11 reports the average NMPC execution time as a function of the RMS value of the yaw rate error, $e_{\dot{\psi}}$, and the peak value of $|\beta|$, for a double lane change from an initial speed of 56 km/h and with $\mu = 0.9$. In all configurations, $|\beta|$ is below the critical threshold of 5 deg, set as a constraint for high tire-road friction conditions, and therefore the controller performance should be evaluated in terms of yaw rate tracking. As $H_P = 500$ ms and $T_S = 20$ ms represent a good compromise between performance and computational effort, with a maximum recorded execution time of 10.81 ms, this controller set-up, indicated by the dashed circles in Fig. 11, was selected for all the following simulations, with $\Delta T = 20$ ms.

E. Cost Function Weight Adaptation

The tuning of the NMPC cost function weights influences the controller behavior. As the NMPC formulation includes two main aspects in J (see (36) and (37)), i.e., yaw rate tracking and power loss reduction, a fuzzy logic weight adaptation algorithm was developed to prioritize energy efficiency during normal driving, and yaw rate tracking as well as rear axle sideslip angle limitation in critical conditions.

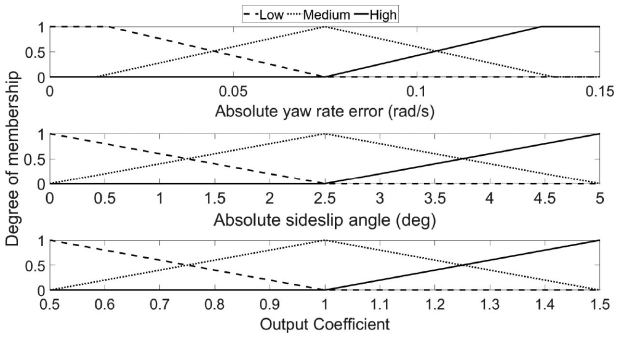

Fig. 12. Fuzzy logic weight adaptation system membership functions.

TABLE II
ADOPTED FUZZY RULES

EO=Energy Oriented YR=Yaw Rate Tracking BW=Balanced Weights		$\lvert e_{\dot{\psi}} \rvert$		
		Low	Medium	High
$\lvert \beta \rvert$	Low	EO	BW	YR
	Medium	EO	BW	YR
	High	EO	YR	YR

TABLE III
COST FUNCTION WEIGHTING COEFFICIENTS

	Yaw Rate Tracking	Energy Oriented	Balanced Weights
r_{u,F_x}	2.5	2.5	2.5
$r_{u,\dot{\psi}}$	5	1	3
$r_{u,\alpha}$	1.5	1.5	1.5
$r_{u,PWT}$	1	5	2.5
$r_{u,Tire}$	1	5	2.5
$r_{u,LD}$	2.5	2.5	2.5

In this proof-of-concept implementation, large values of $|e_{\dot{\psi}}|$ and $|\beta|$ are considered as indicators of undesirable EV behavior. A distribution of three membership functions was chosen for both inputs, $|e_{\dot{\psi}}|$ and $|\beta|$, and for the output coefficient, see Fig. 12. Trapezoidal functions were selected for the boundaries of each variable, while the middle one is triangular. This configuration is computationally efficient (no substantial increase of the computational time was experienced with respect to the values in Fig. 11), while maintaining acceptable response smoothness [50]. The corresponding rules, see Table II, were implemented based on the authors' experience with the system.

During the controller implementation phase, the active safety performance of the NMPC TV system was assessed during obstacle avoidance maneuvers (see Section V for additional details on the test), with four cost function weight configurations (see Table III), i.e., with: i) yaw rate tracking oriented weights, which prioritize vehicle dynamics performance and active safety; ii) energy efficiency oriented weights; iii) balanced weights between energy efficiency and vehicle dynamics; and iv) the fuzzy logic adaptation algorithm.

Fig. 13 shows the resulting EV trajectories for the test from an initial speed of 56 km/h and $\mu = 0.9$. The adaptation mechanism provides an EV response that is very similar to that of case i), focused on vehicle dynamics. Moreover, Table IV reports the maximum speed – the critical speed, V_{cr} – at which each configuration successfully completes the test, i.e., without hitting

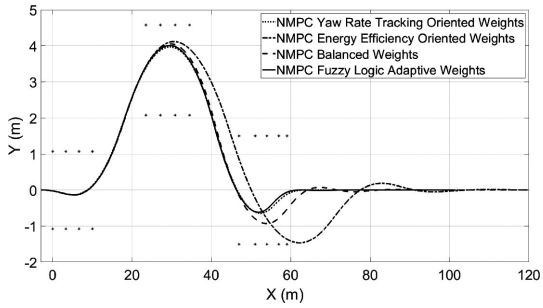

Fig. 13. Double lane change trajectories (initial speed of 56 km/h) associated with different tunings of the NMPC cost function weights ($\mu = 0.9$).

TABLE IV
EFFECT OF COST FUNCTION WEIGHTS ON CRITICAL SPEED FOR OBSTACLE AVOIDANCE

	NMPC Yaw Rate Oriented Weights	NMPC Energy Efficiency Oriented Weights	NMPC Balanced Weights	NMPC Fuzzy Logic Adaptive weights
Critical speed	61 km/h	56 km/h	58 km/h	61 km/h

a cone. In this case, the NMPC with the adaptation mechanism provides the same performance as the vehicle dynamics oriented tuning, corresponding to 5 km/h and 3 km/h higher initial speeds than for the energy-efficiency and balanced tunings. The energy-efficiency benefits of the adaptation with respect to the vehicle dynamics oriented tunings of the controller will be reported in the following Section V.

V. RESULTS

In this section, the NMPC TV system is implemented in the simulation framework defined in Fig. 1, and compared with other controller configurations, which are introduced in Sections V.A and V.B.

A. Analyzed EV Controller Configurations

This section analyzes the performance of the following EV configurations:

- Passive, evenly distributing the torque among the wheels.
- Passive + LUT, providing the same total wheel torque on the two EV sides, i.e., zero direct yaw moment, while the rear-to-total torque distribution within each side is carried out according to the energy-efficient map in Fig. 5.
- Fuzzy + LUT, with a direct yaw moment generated by the fuzzy logic controller in Section V.B, while the rear-to-total torque distribution within each side is carried out according to the energy-efficient map in Fig. 5. This set-up is used as benchmarking TV system in the following analyses.
- NMPC Yaw Rate, i.e., the proposed NMPC TV approach only considering the yaw rate tracking and rear slip angle terms in the cost function, while $W_{u,PWT} = W_{u,Tire} = W_{u,LD} = 0$.
- NMPC PWT Losses, which, on top of the NMPC Yaw Rate features, considers the powertrain power loss term in the cost function, while $W_{u,Tire} = W_{u,LD} = 0$.

- NMPC Tire Losses, i.e., the proposed NMPC TV approach that considers the yaw rate tracking, rear sideslip and tire slip power loss terms in the cost function, while $W_{u,PWT} = W_{u,LD} = 0$.
- NMPC Complete, i.e., the proposed NMPC TV approach that considers yaw rate tracking, rear slip angle, powertrain losses and tire slip power losses, without using the cost function terms related to the rear-to-total wheel torque distribution within each side, i.e., $W_{u,LD} = 0$.
- NMPC Complete WCA, i.e., the proposed NMPC TV approach using all cost function terms, with constant values of the weights.
- NMPC Complete WCA Adaptive, i.e., the proposed NMPC TV approach using all cost function terms, and also including the fuzzy adaptation mechanism of the cost function weights.

B. Benchmarking TV Controller

The proposed NMPC TV is evaluated against the benchmarking TV controller from [19], based on fuzzy logic. The controller uses the Mamdani inference method, as it provides intuitive tuning [51]. With respect to the membership functions, the system considers the yaw rate error, the yaw rate derivative error, and the sideslip angle error. The output is represented by the wheel torque level to be applied to each side of the EV, to generate the direct yaw moment that tracks the reference yaw rate.

A distribution of five membership functions was chosen for the yaw rate error and its derivative, while three membership functions were selected for the sideslip angle. Trapezoidal functions were used for the boundaries of each variable, and also for the middle one of sideslip angle, since the controller tries to minimize this variable, and thus accuracy is not the highest priority. The triangular functions were adopted for all other cases, as they provide computational efficiency while maintaining smooth response, which makes them suitable for implementation in conventional automotive electronic control units (ECUs) [52].

C. Skidpad Tests

50 m radius skid pad simulations for $\mu = 0.9$ and 0.7 were run to assess the relative importance of: a) the reference yaw rate characteristic; and b) the wheel torque control allocation.

The results in Figs. 14 and 15 were obtained by keeping the EV at different constant speeds, each of them corresponding to a marker in the graphs, for several laps. All controllers using the energy-efficient reference yaw rate maps show similar benefits, i.e., relative power input reductions ranging from 5.0% to 6.8% with respect to the Passive configuration. The control allocation layer of the Passive + LUT configuration can reduce the energy consumption only up to 3.6%, with an average saving of 1.8%, and its effect is more significant at low a_y values, corresponding to low speeds. In these conditions the electric powertrains operate in their least efficient region; therefore, the LUT based control allocation algorithm deactivates one of the axles according to the map in Fig. 5, and the torque demand is

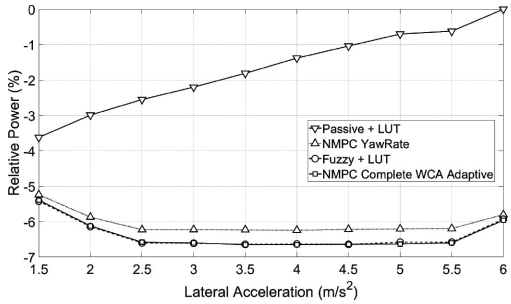

Fig. 14. Percentage power input variation for a selection of configurations, with respect to the Passive configuration, for $\mu = 0.9$.

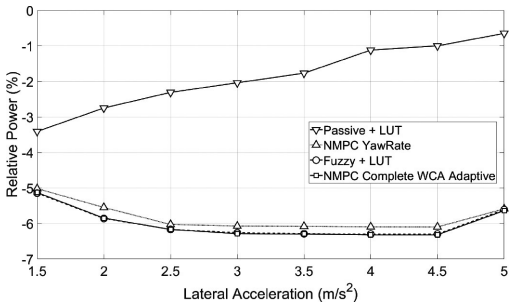

Fig. 15. Percentage power input variation for a selection of configurations, with respect to the Passive configuration, for $\mu = 0.7$.

only provided by the rear axle, which thus operates in a more efficient region. The considerable consumption difference between the Passive + LUT and all the other controlled configurations can be ascribed to the effect of the energy-efficient yaw rate.

In summary, the results show that during steady-state cornering: i) the control allocation aspects of the TV controller, which are the focus of the majority of the existing literature, are less important than the reference yaw rate characteristics; and ii) any TV controller capable of tracking the appropriate energy-efficient reference yaw rate provides rather similar energy consumption results.

Despite the statement in ii), a sophisticated TV algorithm can still provide energy efficiency benefits in specific quasi-steady-state cornering conditions. In fact, as discussed in Section III, the optimal yaw rate reference depends on μ, and thus the friction coefficient estimation is crucial to the correct operation of the algorithm. However, in practice, accurate μ estimation when the EV operates below its friction limits is rather difficult to accomplish. Therefore, a second set of skidpad tests at $\mu = 0.7$ was simulated at a constant a_x of 1 m/s^2, with incorrect ($\mu = 0.9$) and correct ($\mu = 0.7$) friction information provided to the TV controller, to evaluate its ability to compensate for incorrect $\dot{\psi}_{ref}$ profiles.

Fig. 16 visualizes a selection of the resulting EV trajectories. The Fuzzy + LUT configuration is unstable, while the Passive one is affected by significant understeer, with respect to the NMPC TV. Fig. 17 reports the corresponding power consumption results. For the cases with the incorrect yaw rate reference, the power consumption is always greater than for the Passive vehicle, up to ~6% at around 5 m/s^2 for the NMPC Yaw Rate. In contrast, the configurations with the correct yaw rate reference

TABLE V
CRITICAL SPEED ACHIEVED DURING OBSTACLE AVOIDANCE

	Passive	Passive + LUT	Fuzzy + LUT	NMPC Yaw Rate	NMPC PWT Losses	NMPC Tire Losses	NMPC Complete	NMPC Complete WCA	NMPC Complete WCA Adaptive
$\mu = 0.9$	54 km/h	54 km/h	56 km/h	61 km/h	58 km/h	59 km/h	58 km/h	58 km/h	61 km/h
$\mu = 0.7$	37 km/h	37 km/h	40 km/h	45 km/h	42 km/h	45 km/h	43 km/h	43 km/h	45 km/h

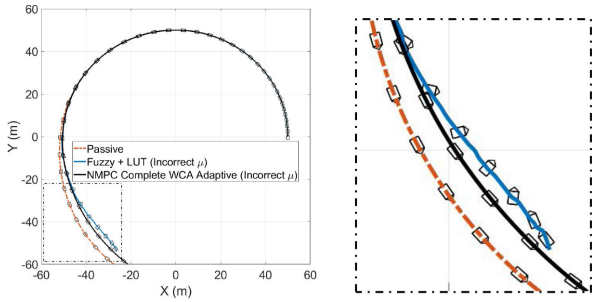

Fig. 16. Skidpad trajectories for a selection of controllers, with $a_x = 1$ m/s^2 and $\mu = 0.7$. The solid boxes indicate the motion of the cars. Left: full maneuver; right: zoom of trajectories towards end of maneuver.

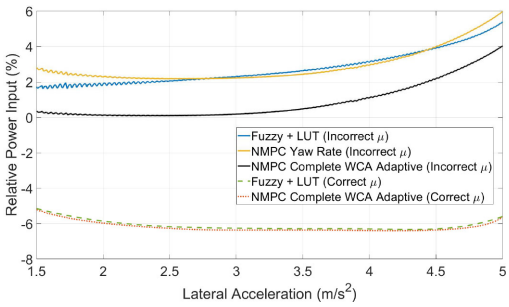

Fig. 17. Percentage power input variation for a selection of controller configurations with respect to the Passive configuration, during a skidpad test with $a_x = 1$ m/s^2 and $\mu = 0.7$.

achieve a power saving of about 6% compared to the Passive case almost across the entire investigated a_y-range. Although the NMPC Complete WCA Adaptive configuration receives the same incorrect ψ_{ref}, its power consumption is lower, on average by ∼2%, than for the other cases with the incorrect ψ_{ref}. In fact, the complex NMPC cost function in (36) and (37) accounts and partially compensates for the increased tire slip power losses caused by the inappropriate reference understeer characteristic.

D. Obstacle Avoidance

The obstacle avoidance, which is frequently used by car makers and supplier to assess vehicle dynamics control systems, was simulated for $\mu = 0.9$ and 0.7, according to the ISO 3888 specification [53]. The vehicle enters the course at a set speed, and the accelerator pedal is released. Then the driver, i.e., the Dynacar driver model in this study, attempts to track the reference path without hitting a cone. The test speed is progressively increased up to its critical value, V_{cr}, at which the course can no longer be successfully negotiated.

Table V reports the V_{cr} values for the Passive vehicle and the controlled configurations, with the best performance being provided by the NMPC Yaw Rate and the NMPC Complete WCA Adaptive, achieving 61 km/h and 45 km/h with the two friction conditions, respectively, against 54 km/h and 37 km/h of the Passive vehicle, and 58 km/h and 43 km/h of the NMPC Complete. The V_{cr} results confirm the functionality of the fuzzy adaptation mechanism.

Figs. 18–23 report a selection of the time profiles of the main variables during obstacle avoidance tests from 56 km/h ($\mu = 0.9$) and 40 km/h ($\mu = 0.7$), which are the lowest critical

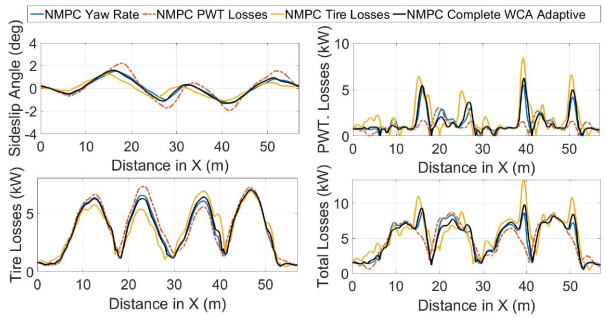

Fig. 18. Power loss profiles during an obstacle avoidance test, for $\mu = 0.9$ and an initial speed of 56 km/h.

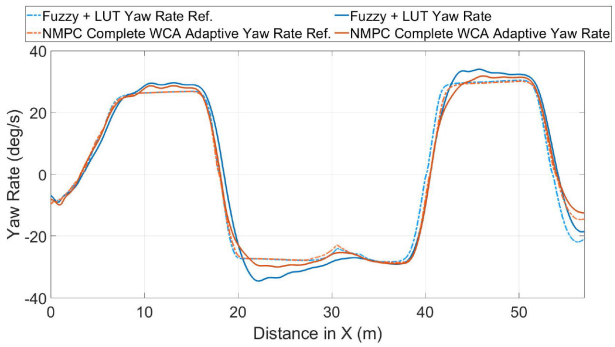

Fig. 19. Yaw rate tracking performance during an obstacle avoidance test, for $\mu = 0.9$ and an initial speed of 56 km/h.

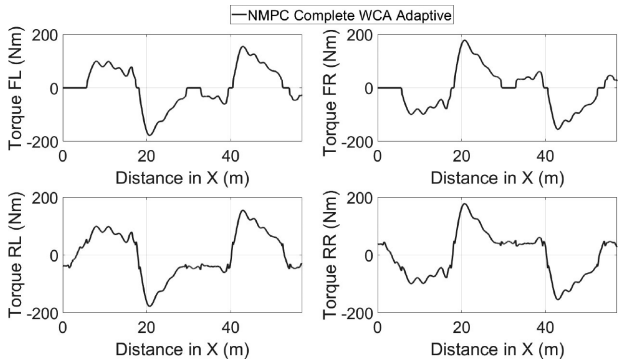

Fig. 20. Motor torques profiles during an obstacle avoidance test, for $\mu = 0.9$ and an initial speed of 56 km/h.

Figs. 18–23 report a selection of the time profiles of the main variables during obstacle avoidance tests from 56 km/h ($\mu = 0.9$) and 40 km/h ($\mu = 0.7$), which are the lowest critical

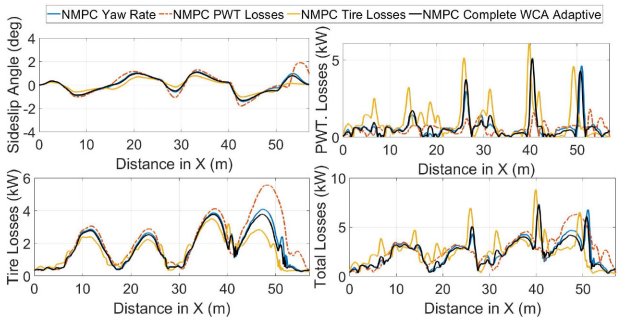

Fig. 21. Power loss profiles during an obstacle avoidance test, for $\mu = 0.7$ and an initial speed of 40 km/h.

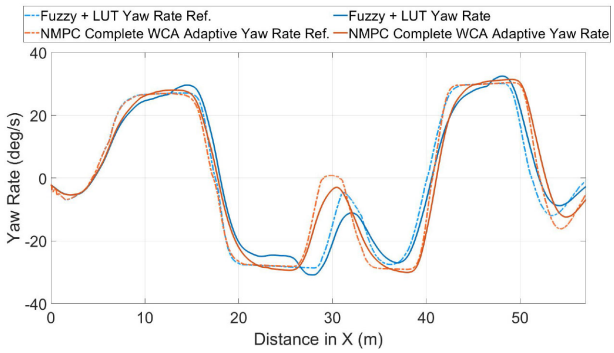

Fig. 22. Yaw rate tracking during an obstacle avoidance test, for $\mu = 0.7$ and an initial speed of 40 km/h.

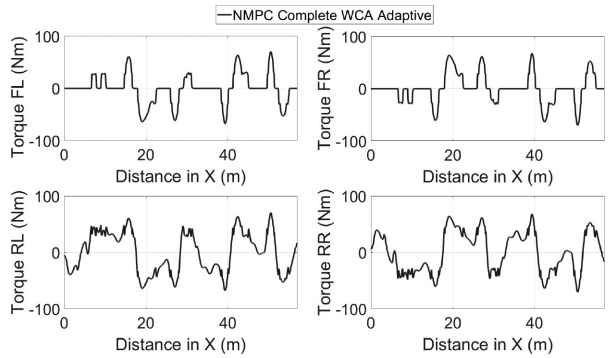

Fig. 23. Motor torques profiles during an obstacle avoidance test, for $\mu = 0.7$ and an initial speed of 40 km/h.

speeds of the controlled vehicle for the respective μ, achieved by the Fuzzy + LUT set-up. In particular, Figs. 18 and 21 show the vehicle sideslip angle, powertrain power losses, the sum of the longitudinal and lateral tire slip power losses, and the total TV-affected power losses for four TV controller configurations. Figs. 19 and 22 plot the yaw rate tracking performance for the Fuzzy + LUT and NMPC Complete WCA Adaptive set-ups. Figs. 20 and 23 show the profiles of the four wheel torques for the NMPC Complete WCA Adaptive configuration. The inclusion of the tire slip power loss term in the NMPC cost function reduces the sideslip angle, as β is directly related to the tire slip angles (see (28)), and the lateral tire slip power losses (see (6)). As expected, the combination of all cost function terms brings the most balanced, and therefore, most efficient result.

Tables VI and VII include the values of objective performance indicators to assess the performance of the different configurations during the two considered obstacle avoidance tests. The adopted indicators are:

- The final vehicle speed, V_{fin}, i.e., the speed at the exit of the course, which is an indicator of vehicle agility and the level of tire slip power loss.
- The root mean square value of the yaw rate error, $RMS(e_{\dot{\psi}})$, which evaluates the yaw rate tracking performance and vehicle agility.
- The peak absolute value of the rear axle slip angle, $|\alpha_{R,max}|$, which assesses vehicle stability as well as tire slip power losses.
- The normalized integral of the absolute value of the steering angle δ_{SW}:

$$IA_{\delta_{SW}} = \frac{1}{t_{fin} - t_{in}} \int_{t_{in}}^{t_{fin}} |\delta_{SW}|\, dt \tag{38}$$

where t_{in} and t_{fin} are the initial and final times of the relevant part of the test, calculated when the EV enters and leaves the obstacle avoidance course. $IA_{\delta_{SW}}$ assesses the required steering effort to follow the reference path.

- The normalized integral of the absolute value of the reference direct yaw moment, $M_{z,ref}$, calculated from the individual reference wheel torque demands:

$$IA_{M_{z,ref}} = \frac{1}{t_{fin} - t_{in}} \int_{t_{in}}^{t_{fin}} |M_{z,ref}|\, dt \tag{39}$$

The results confirm the superior performance of the NMPC Complete WCA Adaptive, which has the highest V_{fin} in both tests (ultimate proof of reduced power loss), and consistently good performance in all other indicators. The results also highlight that energy-efficient TV control should account for both powertrain and tire slip power losses to achieve energy saving in a wide range of vehicle operation. For $\mu = 0.9$, V_{fin} is comparable for the NMPC PWT Losses and NMPC Tire Losses configurations, while for $\mu = 0.7$ the latter configuration is significantly more efficient.

To show the robustness of the NMPC WCA Adaptive set-up with respect to the Passive configuration, Table VIII reports the values of $RMS(e_{\dot{\psi}})$ and $|\alpha_{R,max}|$ for obstacle avoidance tests at $\mu = 0.9$, from 50 km/h, with significant variations (given the specific vehicle category) of the vehicle inertial parameters. The results confirm that the proposed controller provides safe performance for any inertial condition, while the Passive set-up, which is still stable with the nominal inertial parameters, experiences a major increase in $|\alpha_{R,max}|$, which exceeds 30 deg for the most extreme variation of inertial parameters. Hence, based on this analysis and the one in Figs. 16 and 17, it can be confidently concluded that the proposed controller is robust with respect to a very wide range of operating conditions of the vehicle.

E. Driving Cycles

Driving cycle simulations were run to evaluate the effect of the rear-to-total wheel torque distribution during straight-line

TABLE VI
OBSTACLE AVOIDANCE RESULTS FOR $\mu = 0.9$ AND 56 km/h

	Fuzzy + LUT	NMPC Yaw Rate	NMPC PWT Losses	NMPC Tire Losses	NMPC Complete	NMPC Complete WCA	NMPC Complete WCA Adaptive
V_{fin} (km/h)	42.39	44.04	44.17	44.75	44.46	44.29	45.40
$RMS(e_{\dot{\psi}})$ (deg/s)	2.32	1.52	2.57	1.88	1.88	1.96	1.60
$\lvert\alpha_{R,max}\rvert$ (deg)	3.08	4.80	5.02	4.33	4.82	4.57	4.16
$IA_{\delta_{SW}}$ (deg)	45.87	48.09	52.73	54.60	51.43	53.38	44.91
$IA_{M_{z,ref}}$ (Nm)	410.31	402.69	380.25	391.06	391.89	399.98	368.96

TABLE VII
OBSTACLE AVOIDANCE RESULTS FOR $\mu = 0.7$ AND 40 km/h

	Fuzzy + LUT	NMPC Yaw Rate	NMPC PWT Losses	NMPC Tire Losses	NMPC Complete	NMPC Complete WCA	NMPC Complete WCA Adaptive
V_{fin} (km/h)	30.58	32.80	31.76	34.06	33.86	33.10	34.17
$RMS(e_{\dot{\psi}})$ (deg/s)	3.48	1.32	2.91	1.29	1.60	1.67	1.34
$\lvert\alpha_{R,max}\rvert$ (deg)	4.14	3.36	3.60	2.93	3.54	3.49	3.04
$IA_{\delta_{SW}}$(deg)	68.97	42.23	56.25	32.95	45.11	47.85	42.27
$IA_{M_z,ref}$ (Nm)	255.41	179.54	168.11	275.68	179.95	191.27	181.00

TABLE VIII
OBSTACLE AVOIDANCE RESULTS FOR $\mu = 0.9$ AND 50 km/h, FOR DIFFERENT INERTIAL PARAMETERS OF THE VEHICLE

	m = 649 kg, I_z = 400 kg m^2, l_f = 0.99 m		m = 679 kg, I_z = 475 kg m^2, l_f = 1.05 m		m = 699 kg, I_z = 600 kg m^2, l_f = 0.90 m		m = 719 kg, I_z = 675 kg m^2, l_f = 0.85 m		m =749 kg, I_z = 800 kg m^2, l_f = 0.90 m	
	Passive	NMPC Complete WCA Adaptive	Passive	NMPC Complete WCA Adaptive	Passive	NMPC Complete WCA Adaptive	Passive	NMPC Complete WCA Adaptive	Passive	NMPC Complete WCA Adaptive
$RMS(e_{\dot{\psi}})$ (deg/s)	9.9	1.5	13.1	2.2	15.0	2.6	20.2	3.1	33.3	4.6
$\lvert\alpha_{R,max}\rvert$ (deg)	7.35	3.81	8.17	4.24	9.61	4.69	11.15	4.85	31.72	5.30

operation. The selected cycles (World harmonized Light Vehicles Test Procedure (WLTP), excluding the extra high speed section; New European Driving Cycle (NEDC); ARTEMIS road; and ARTEMIS urban, see [54]-[56]) cover a wide range of longitudinal speeds and accelerations, corresponding to urban and extra-urban driving conditions.

The total powertrain energy consumption, E_{tot}, is calculated as:

$$E_{tot} = \int_{t_{in}}^{t_{fin}} \sum_{\substack{i=F,R \\ j=R,L}} \left(\tau_{ij}\omega_{ij} + P_{Loss,PWT,ij}\right) dt \qquad (40)$$

where (40) considers only the energy consumed by the electric powertrains, and neglects the energy consumption of the vehicle ancillaries, such as the lights or the air conditioning system.

The results are reported in Table IX only for the most advanced NMPC set-up, as the energy consumption is very similar with all controlled configurations. This outcome is expected, considering the nature of the mission profiles, involving EV operation only in straight-line, the low torque levels, and, thus, the low longitudinal tire slip values. Hence, the energy consumption during the driving cycles is dominated by the powertrain power loss characteristics.

For all schedules, the NMPC Complete WCA Adaptive leads to reduced energy consumption with respect to the single axle configuration, using only the rear powertrains (while the front powertrains are switched off), and the even distribution strategy, i.e., the Passive configuration defined in Section V.A. Depending on the driving cycle, the saving of the NMPC TV implementation ranges between 0.21% and 2.46%, with an average saving of 1.06%, with respect to the single axle case, and between 0.47% and 3.18%, with an average saving of 2.04%, compared to the even distribution configuration. The results are aligned with those in other recent energy-efficient rear-to-total wheel torque distribution studies [35], [36].

TABLE IX
ENERGY CONSUMPTION RESULTS ALONG A SELECTION OF DRIVING CYCLES

	Energy consumption (kWh)			Improvement (%) of NMPC with respect to	
Driving Cycle	Single Axle	Even Distribution	NMPC Complete WCA Adaptive	Single Axle	Even Distribution (Passive)
WLTP	1.433	1.477	1.43	0.21	3.18
NEDC	0.593	0.604	0.589	0.77	2.58
ARTEMIS-road	1.985	2.008	1.969	0.8	1.94
ARTEMIS-urban	0.495	0.485	0.483	2.46	0.47

F. Circuit

The final test assesses the controllers in a complex scenario, i.e., the circuit of the 2015 Formula Student Germany competition. Fig. 24 shows the vehicle path along the track, and the fixed speed profile followed by all controller configurations, which

TABLE X
PERFORMANCE INDICATORS OF THE EV CONFIGURATIONS ALONG THE SELECTED CIRCUIT

	Passive	Passive + LUT	Fuzzy + LUT	NMPC Yaw Rate	NMPC PWT Losses	NMPC Tire Losses	NMPC Complete	NMPC Complete WCA	NMPC Complete WCA Adaptive
Energy consumption (kWh)	1.178	1.171	1.132	1.118	1.095	1.103	1.072	1.070	1.067
En. cons. variation w.r.t Passive (%)	-	-0.59	-3.93	-5.13	-7.06	-6.38	-9.01	-9.16	-9.43
$RMS(e_{\dot{\psi}})$ (deg/s)	4.75	4.76	2.69	1.90	2.33	2.04	2.10	2.12	1.93
$IA_{\delta_{SW}}$ (deg)	41.27	41.35	37.88	36.16	38.76	36.46	37.55	37.71	36.00
$IA_{\delta_{SW}}$ variation w.r.t. Passive (%)	-	+0.20	-8.21	-12.37	-6.06	-11.65	-9.01	-8.62	-12.75

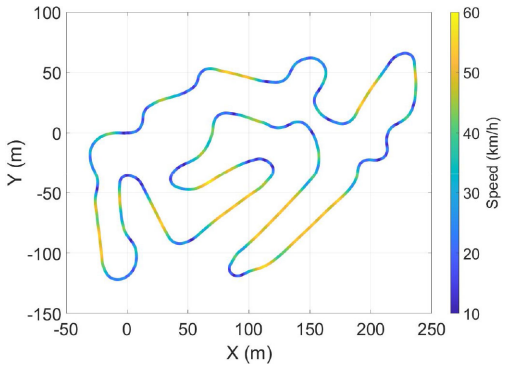

Fig. 24. Vehicle path along the circuit of the 2015 Formula Student Germany competition; colors indicate the fixed speed profile along the track.

corresponds to a rather "aggressive" driving style within the limit of handling, with peak values of lateral acceleration of $\sim$6 m/s^2.

Table X reports the main performance indicators. The fast driving style does not allow the LUT based control allocation to bring substantial benefits, which is confirmed by the energy saving of only 0.59% of the Passive + LUT with respect to the Passive. Thanks to the adoption of an energy-efficient reference yaw rate characteristic, the Fuzzy + LUT achieves a 3.93% energy consumption reduction with respect to the Passive configuration.

Importantly, all NMPC implementations, including the NMPC Yaw Rate, consume less than the benchmarking Fuzzy + LUT set-up. In fact, although the NMPC Yaw Rate formulation does not consider the power loss contributions or the energy-efficient rear-to-total wheel torque distribution within its cost function, it provides significantly better yaw rate tracking performance than the Fuzzy + LUT, which is beneficial to both active safety and consumption. The energy saving is very similar for the NMPC PWT Losses and the NMPC Tire Losses, i.e., $\sim$6-7%, while all NMPC configurations that consider all power loss terms in ł reduce the consumption by more than 9%. In general, these results confirm the importance of the reference understeer characteristic on the EV energy consumption.

The implementation of energy-efficient TV configurations does not compromise the vehicle cornering response with respect to the Passive vehicle; on the contrary, despite achieving higher stability, i.e., larger values of V_{cr} in the obstacle avoidance tests, the energy-efficient TV controlled configurations alleviate the steering effort, with $IA_{\delta_{SW}}$ reductions ranging from 6% to nearly 13%.

G. Summary and Discussion

The results of the extensive simulation analysis on a case-study lightweight electric vehicle with in-wheel motors can be summarized as follows:

- In quasi-steady-state cornering conditions, the reference understeer characteristic has more influence on the energy consumption than the control allocation algorithm (see Figs 14 and 15 in Section V.C). This effect is progressively more evident with increasing lateral acceleration.
- Although the inclusion of the power loss terms in the TV controller formulation only marginally improves the power consumption during steady-state cornering, it significantly enhances system robustness by compensating for the power consumption increase caused by state estimation errors, e.g., on the tire-road friction coefficient (see Figs. 16 and 17 in Section V.C).
- The adaptation mechanism of the cost function weights of the nonlinear model predictive controller formulation provides significant operational flexibility with respect to the actual driving situation, i.e., by prioritizing energy efficiency during normal driving, and vehicle safety and stability in extreme maneuvers. With such mechanism, the NMPC TV system is characterized by the same critical speed in obstacle avoidance maneuvers as its version tuned only for vehicle dynamics performance, i.e., 61 km/h at $\mu = 0.9$ and 45 km/h at $\mu = 0.7$, against 54 km/h and 37 km/h for the Passive configuration, and 56 km/h and 40 km/h for the benchmarking Fuzzy + LUT controller (see Section V.D).
- With respect to the Passive configuration, the most advanced control configuration proposed in this study, the NMPC Complete WCA Adaptive, reduces energy consumption by $\sim$2% on average during the selected driving cycles in straight-line conditions (see Section V.E), and $\sim$9% along the considered circuit (see Section V.F). Also, along the circuit, the NMPC Complete WCA Adaptive brings a consumption reduction in excess of 5% with respect to the Fuzzy + LUT set-up, which is a remarkable energy saving, given that the benchmarking controller uses energy-efficient reference yaw rate and rear-to-total wheel torque distribution.

VI. CONCLUSION

This study presented a set of nonlinear model predictive controllers for electric vehicles with multiple powertrains,

targeting energy efficiency enhancement through the appropriate control of the cornering response and wheel torque allocation, with formulations considering powertrain power losses and tire slip power losses, while providing the expected level of vehicle dynamics performance.

Comprehensive results showed the significant positive impact of the generated energy-efficient reference yaw rate map on energy consumption in steady-state cornering conditions. Such improvement was evident also for the benchmarking controller, i.e., a torque-vectoring system based on a fuzzy logic implementation, coupled with an energy-efficient control allocation layer. Nevertheless, the inclusion of the different relevant power loss contributions in the cost function terms of the developed NMPC formulations allows to compensate for inaccuracies, e.g., related to the estimation of the tire-road friction coefficient in the online generation of the energy-efficient reference yaw rate, and for the effect of cornering transients, thus providing robustness to the energy efficiency enhancement.

A single NMPC setting was unable to concurrently provide the best energy consumption performance in normal driving conditions, and the safest cornering response during emergency maneuvers, e.g., obstacle avoidance tests. Therefore, the paper presented an adaptation mechanism of the NMPC weights, which was implemented in the most advanced proposed controller configuration, i.e., the NMPC TV WCA Adaptive, which provided the most significant improvements in all considered scenarios, thanks to its operational flexibility in prioritizing the energy efficiency or vehicle dynamics aspects.

Future developments will include the experimental assessment of the developed NMPC algorithms on electric vehicle demonstrators, and their extension to vehicle plants with additional chassis control actuators.

REFERENCES

[1] S. Manzetti and F. Mariasu, "Electric vehicle battery technologies: From present state to future systems," *Renewable Sustain. Energy Rev.*, vol. 51, pp. 1004–1012, 2015.

[2] Accessed: Jan. 3, 2020. [Online]. Available: https://ionity.eu/

[3] Accessed: Jan. 3, 2020. [Online]. Available: https://www.tesla.com/en_GB/supercharger

[4] W. Dib, A. Casse, P. Moulin, A. Sciarretta, and G. Corde, "Optimal energy management for an electric vehicle in eco-driving application," *Control Eng. Practice*, vol. 29, pp. 299–307, 2014.

[5] Y. Wang, B. M. Nguyen, H. Fujimoto, and Y. Hori, "Multirate estimation and control of body sideslip angle for electric vehicles based on onboard vision system," *IEEE Trans. Ind. Electron.*, vol. 61, no. 2, pp. 1133–1143, Feb. 2014.

[6] B. Lenzo, A. Sorniotti, P. Gruber, and K. Sannen, "On the experimental analysis of single input single output control of yaw rate and sideslip angle," *Int. J. Automot. Technol.*, vol. 18, no. 5, pp. 799–811, 2017.

[7] A. Wong, D. Kasinathan, A. Khajepour, S. K. Chen, and B. Litkouhi, "Integrated torque vectoring and power management framework for electric vehicles," *Control Eng. Practice*, vol. 48, pp. 22–36, 2016.

[8] R. de Castro , M. Tanelli, R. E. Araújo , and S. M. Savaresim "Minimum-time manoeuvring in electric vehicles with four wheel-individual-motors," *Veh. Syst. Dyn.*, vol. 52, no. 6, pp. 824–846, 2014.

[9] E. N. Smith, D. Tavernini, E. Velenis, and D. Cao, "Evaluation of optimal yaw rate reference for closed-loop electric vehicle torque vectoring," in *Proc. 13th Int. Symp. Adv. Veh. Control (AVEC'16)*, pp. 619–624, 2016.

[10] V. Ivanov, D. Savitski, and B. Shyrokau, "A survey of traction control and antilock braking systems of full electric vehicles with individually controlled electric motors," *IEEE Trans. Veh. Technol.*, vol. 64, no. 9, pp. 3878–3896, Sep. 2015.

[11] L. De Novellis, A. Sorniotti, and P. Gruber, "Driving modes for designing the cornering response of fully electric vehicles with multiple motors," *Mech. Syst. Signal Process.*, vol. 64–65, pp. 1–15, 2015.

[12] L. De Novellis *et al.*, "Direct yaw moment control actuated through electric drivetrains and friction brakes: Theoretical design and experimental assessment," *Mechatronics*, vol. 26, pp. 1–15, 2015.

[13] L. De Novellis, A. Sorniotti, P. Gruber, and A. Pennycott, "Comparison of feedback control techniques for torque-vectoring control of fully electric vehicles," *IEEE Trans. Veh. Technol.*, vol. 63, no. 8, pp. 3612–3623, Oct. 2014.

[14] Q. Lu *et al.*, "Enhancing vehicle cornering limit through sideslip and yaw rate control," *Mech. Syst. Signal Process.*, vol. 75, pp. 455–472, 2016.

[15] Q. Lu, A. Sorniotti, P. Gruber, J. Theunissen, and J. De Smet, "H∞ loop shaping for the torque-vectoring control of electric vehicles: Theoretical design and experimental assessment," *Mechatronics*, vol. 35, pp. 32–43, 2016.

[16] T. Goggia *et al.*, "Integral sliding mode for the torque-vectoring control of fully electric vehicles: Theoretical design and experimental assessment," *IEEE Trans. Veh. Technol.*, vol. 64, no. 5, pp. 1701–1715, May 2015.

[17] A. Tota *et al.*, "On the experimental analysis of integral sliding modes for yaw rate and sideslip control of an electric vehicle with multiple motors," *Int. J. Automot. Technol.*, vol. 19, no. 5, pp. 811–823, 2018.

[18] E. Esmailzadeh, A. Goodarzi, and G. R. Vossoughi, "Optimal yaw moment control law for improved vehicle handling," *Mechatronics*, vol. 13, no. 7, pp. 659–675, 2003.

[19] A. Parra, A. Zubizarreta, J. Perez, and M. Dendaluce, "Intelligent torque-vectoring approach for electric vehicles with per-wheel motors," *Complexity*, pp. 1–14, 2018, Art. no. 7030184.

[20] E. Siampis, E. Velenis, S. Gariuolo, and S. Longo, "A real-time nonlinear model predictive control strategy for stabilization of an electric vehicle at the limits of handling," *IEEE Trans. Control Syst. Technol.*, vol. 26, no. 6, pp. 1982–1994, Nov. 2019.

[21] E. Siampis, E. Velenis, and S. Longo, "Rear wheel torque vectoring model predictive control with velocity regulation for electric vehicles," *Veh. Syst. Dyn.*, vol. 53, no. 11, pp. 1555–1579, 2015.

[22] M. Ataei, A. Khajepour, and S. Jeon, "Model predictive control for integrated lateral stability, traction/braking control, and rollover prevention of electric vehicles," *Veh. Syst. Dyn.*, vol. 58, no. 1, pp. 49–73, 2020.

[23] T. Kobayashi, E. Katsuyama, H. Sugiura, E. Ono, and M. Yamamoto, "Direct yaw moment control and power consumption of in-wheel motor vehicle in steady-state turning," *Veh. Syst. Dyn.*, vol. 55, pp. 104–120, 2017.

[24] T. Kobayashi, E. Katsuyama, H. Sugiura, E. Ono, and M. Yamamoto, "Efficient direct yaw moment control: Tyre slip power loss minimisation for four-independent wheel drive vehicle," *Veh. Syst. Dyn.*, vol. 56, pp. 1–15, 2017.

[25] J. Edrén, J. Jerrelind, A. Trigell, L. Drugge, and M. Jonasson, "Energy efficient cornering using over-actuation," *Mechatronics*, vol. 59, pp. 69–81, 2019.

[26] A. Tahouni, M. Mirzaei, and B. Najjari, "Novel constrained nonlinear control of vehicle dynamics using integrated active torque vectoring and electronic stability control," *IEEE Trans. Veh. Technol.*, vol. 68, no. 10, pp. 9564–9572, Oct. 2019.

[27] G. Chen, M. Hua, C. Zong, B. Zhang, and Y. Huang, "Comprehensive chassis control strategy of FWIC-EV based on sliding mode control," *IET Intell. Transp. Syst.*, vol. 13, no. 4, pp. 703–713, 2019.

[28] H. Peng, W. Wang, C. Xiang, L. Li, and X. Wang, "Torque coordinated control of four in-wheel motor independent-drive vehicles with consideration of the safety and economy," *IEEE Trans. Veh. Technol.*, vol. 68, no. 10, pp. 9604–9618, Oct. 2019.

[29] C. Lin, S. Liang, J. Chen, and X. Gao, "A multi-objective optimal torque distribution strategy for four in-wheel-motor drive electric vehicles," *IEEE Access*, vol. 7, pp. 64627–64640, 2019.

[30] B. Zhao, N. Xu, H. Chen, K. Guo, and Y. Huang, "Stability control of electric vehicles with in-wheel motors by considering tire slip energy," *Mech. Syst. Signal Process.*, vol. 118, pp. 340–359, 2019.

[31] A. Pennycott, L. De Novellis, A. Sabbatini, P. Gruber, and A. Sorniotti, "Reducing the motor power losses of a four-wheel drive, fully electric vehicle via wheel torque allocation," *Proc. Inst. Mech. Eng. Part D: J. Automobile Eng.*, vol. 228, no. 7, pp. 830–839, 2014.

[32] Z. Li, R. Hou, T. Sun, and S. Kavuma, "Continuous steering stability control based on an energy-saving torque distribution algorithm for a four in-wheel-motor independent-drive electric vehicle," *Energies*, vol. 11, no. 2, 2018, Art. no. 350.

[33] Y. Chen and J. Wang, "Design and experimental evaluations on energy efficient control allocation methods for overactuated electric vehicles: Longitudinal motion case," *IEEE/ASME Trans. Mechatronics*, vol. 19, no. 2, pp. 538–548, Apr. 2014.
[34] B. Lenzo *et al.*, "Torque distribution strategies for energy-efficient electric vehicles with multiple drivetrains," *ASME. J. Dyn. Syst. Meas. Control*, vol. 139, no. 12, 2017.
[35] A. M. Dizqah, B. Lenzo, A. Sorniotti, P. Gruber, S. Fallah, and J. De Smet, "A fast and parametric torque distribution strategy for four-wheel-drive energy-efficient electric vehicles," *IEEE Trans. Ind. Electron.*, vol. 63, no. 7, pp. 4367–4376, Jul. 2016.
[36] A. M. Dizqah, B. L. Ballard, M. V. Blundell, S. Kanarachos, and M. S. Innocente, "A non-convex control allocation strategy as energy-efficient torque distributors for on-road and off-road vehicles," *Control Eng. Practice*, vol. 95, 2020, Art. no. 104256.
[37] G. De Filippis, B. Lenzo, A. Sorniotti, P. Gruber, K. Sannen, and J. De Smet, "On the energy efficiency of electric vehicles with multiple motors," in *Proc. IEEE Veh. Power Propulsion Conf. (VPPC)*, 2016, pp. 1–6.
[38] G. De Filippis, B. Lenzo, A. Sorniotti, P. Gruber, and W. De Nijs, "Energy-efficient torque-vectoring control of electric vehicles with multiple drivetrains," *IEEE Trans. Veh. Technol.*, vol. 67, no. 6, pp. 4702–4715, Jun. 2018.
[39] C. Chatzikomis *et al.*, "An energy-efficient torque-vectoring algorithm for electric vehicles with multiple motors," *Mech. Syst. Signal Process.*, vol. 128, pp. 655–673, 2019.
[40] "Dynacar by Tecnalia," Accessed: Jan. 5, 2020. [Online]. Available: http://www.dynacar.es/en/home.php
[41] A. Parra, D. Cagigas, A. Zubizarreta, A. J. Rodríguez, and P. Prieto, "Modelling and validation of full vehicle model based on a novel multibody formulation," in *Proc. IECON 45th Annu. Conf. IEEE Ind. Electron. Soc.*, 2019, pp. 675–680.
[42] M. Dendaluce, I. Iglesias, A. Martin, P. Prieto, and A. Pena, "Race-track testing of a torque vectoring algorithm on a motor-in-wheel car using a model-based methodology with a hil and multibody simulator setup," in *Proc. Int. Conf. Intell. Transp. Syst.*, 2016, pp. 2500–2505.
[43] J. Cuadrado, D. Dopico, M. Gonzalez, and M. A. Naya, "A combined penalty and recursive real-time formulation for multibody dynamics," *J. Mech. Design*, vol. 126, no. 4, pp. 602–608, 2004.
[44] H. B. Pacejka, in *Tire and Vehicle Dynamics*. 2nd ed., Oxford: Butterworth-Heinemann, 2006.
[45] Elaphe Propulsion Technologies Ltd. Accessed: Jan. 16, 2020. [Online]. Available: http://in-wheel.com/en/
[46] T. D. Gillespie, in *Fundamentals of Vehicle Dynamics*. Warrendale, PA, USA: SAE International, 1996.
[47] W. F. Milliken and D. L. Milliken, in *Race Car Vehicle Dynamics*. Warrendale, PA, USA: SAE International, 1996.
[48] L. Grüne and J. Pannek, in *Nonlinear Model Predictive Control*. Berlin, Germany: Springer, 2011.
[49] B. Houska, H. J. Ferreau, and M. Diehl, "An auto-generated real-time iteration algorithm for nonlinear MPC in the microsecond range," *Automatica*, vol. 47, no. 10, pp. 2279–2285, 2011.
[50] Y. Bai and D. Wang, "Fundamentals of fuzzy logic control - fuzzy sets, fuzzy rules and defuzzifications," in *Advanced Fuzzy Logic Technologies in Industrial Applications, Advances in Industrial Control*. Berlin, Germany: Springer, 2006.
[51] M. Blej and M. Azizi, "Comparison of mamdani-type and sugeno-type fuzzy inference systems for fuzzy real time scheduling," *Int. J. Appl. Eng. Res.*, vol. 5, no. 5, pp. 11071–11075, 2016.
[52] Y. Bai and D. Wang, "Fundamentals of fuzzy logic control - fuzzy sets, fuzzy rules and defuzzifications," in *Advanced Fuzzy Logic Technologies in Industrial Applications, Advances in Industrial Control*. Berlin, Germany: Springer, 2006.
[53] ISO 3888-2:2011 Passenger cars – Test track for a severe lane-change manoeuvre – Part 2: Obstacle avoidance.
[54] "Worlwide, harmonized Light vehicles Test Procedure," Accessed: Jan. 9, 2020. [Online]. Available: https://wiki.unece.org/pages/viewpage.action?pageId = 2523179
[55] J. Demuynck, D. Bosteels, M. De Paepe, C. Favre, J. May, and S. Verhelst, "Recommendations for the new WLTP cycle based on an analysis of vehicle emission measurements on NEDC and CADC," *Energy Policy*, vol. 49, pp. 234–242, 2012.
[56] M. André, "The ARTEMIS European driving cycles for measuring car pollutant emissions," *Sci. Total Environ.*, vol. 334–335, pp. 73–83, 2004.

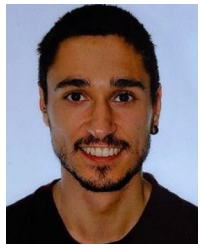

Alberto Parra received the B.Sc. degree in automatics and industrial electronics engineering and the M.Sc. degree in control engineering, automation, and robotics from the University of the Basque Country, Bilbao, Spain, in 2015 and 2017, respectively. He is a Ph.D. Researcher with Tecnalia Research & Innovation and the University of the Basque Country. His research interests include vehicle dynamics modeling and control, and automated driving.

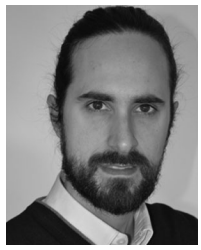

Davide Tavernini received the M.Sc. degree in mechanical engineering and the Ph.D. degree in dynamics and design of mechanical systems from the University of Padova, Padua, Italy, in 2010 and 2014. During the Ph.D. degree, he was part of the motorcycle dynamics research group. He is a Lecturer in advanced vehicle engineering with the University of Surrey, Guildford, U.K. His research interests include vehicle dynamics modeling and control, mostly applied to electric and hybrid electric vehicles.

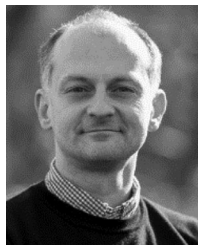

Patrick Gruber received the M.Sc. degree in motorsport engineering and management from Cranfield University, Cranfield, U.K., in 2005, and the Ph.D. degree in mechanical engineering from the University of Surrey, Guildford, U.K., in 2009. He is a Reader in advanced vehicle systems engineering with the University of Surrey. His research interests include vehicle dynamics and tire dynamics with special focus on friction behavior.

Aldo Sorniotti (Member, IEEE) received the M.Sc. degree in mechanical engineering and Ph.D. degree in applied mechanics from the Politecnico di Torino, Turin, Italy, in 2001 and 2005, respectively. He is a Professor in advanced vehicle engineering with the University of Surrey, Guildford, U.K., where he coordinates the Centre for Automotive Engineering. His research interests include vehicle dynamics control and transmission systems for electric and hybrid electric vehicles.

Asier Zubizarreta received the Ph.D. degree in robotics and automatic control systems from the University of the Basque Country (UPV/EHU), Bilbao, Spain, in 2010. He is currently an Associate Professor with the Department of Automatic Control and Systems Engineering, Faculty of Engineering of UPV/EHU, Bilbao. He has worked in several projects in the areas of robotics, virtual sensors, and model-based predictive control. Since 2012, he has been leading the Formula Student Bizkaia Project. He is focused on the development of virtual sensors and MPC-based controllers for automated driving.

Joshué Pérez (Member, IEEE) received the B.Eng. degree in electronic engineering from the Simon Bolívar University, Venezuela, in 2007. He received the M.Eng. and Ph.D. degrees from the University Complutense of Madrid, Madrid, Spain, in 2009 and 2012, respectively. He has been a Research Leader on Automated Driving at Tecnalia Research and Innovation, since 2015. He has more than 11 years of experience in the Intelligent Transportation Systems field, and more than 120 publications related to automated driving and advanced driver-assistance systems.